Orbital Hybridization States of Carbon Function the Alkali-Ion Storage Capability of Hard Carbons

Ying Yang[a], Chenli Huang[b], Ruirui Zhao[a], Zhonghui Gao[a], Xiaoqun Qi[a], Wang Zhang[c], Xing Lu[b *], Long Qie[b *], and Yunhui Huang[b *]

[a]Institute of New Energy for Vehicles, School of Materials Science and Engineering, Tongji University, Shanghai, 201804, China.

[b]State Key Laboratory of Material Processing and Die & Mold Technology, School of Materials Science and Engineering, Huazhong University of Science and Technology, Wuhan, Hubei Province, 430074, China.

[c]Institute for Superconducting and Electronic Materials, University of Wollongong, Wollongong, NSW 2522, Australia.

Y. Ying and C. Huang contributed equally to this work.

*Corresponding authors. E-mail: lux@hust.edu.cn, qie@hust.edu.cn, and huangyh@hust.edu.cn

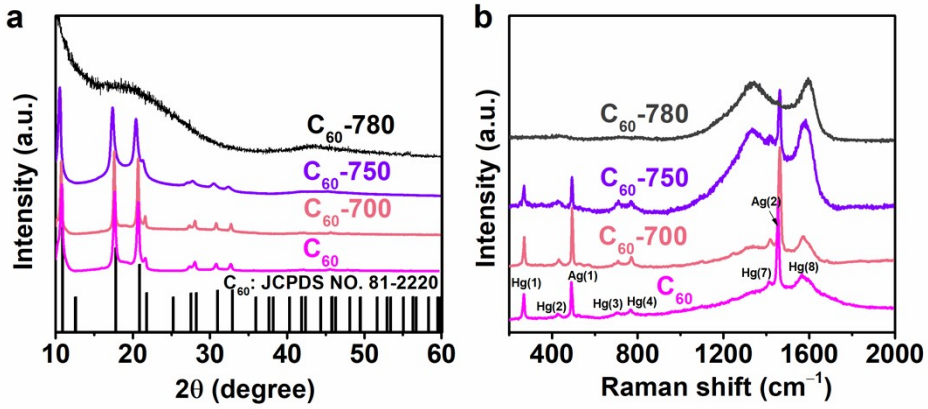

Fig. S1 The conformation of carbonization temperature for synthesizing HCs. a The XRD patterns of C_{60}, C_{60}-700, C_{60}-750, and C_{60}-780 samples. **b** The Raman spectra of C_{60}, C_{60}-700, C_{60}-750, and C_{60}-780 samples.

To find the transforming temperature from C_{60} to hard carbons, we conduct a series of experiments at various annealing temperatures from 700, 750, 780, 800, 900, to 1000 °C. The XRD patterns and Raman spectra of C_{60} and C_{60}-T samples at 700, 750, and 780 °C are added and shown in Fig. S1. It could be seen that all the peaks of C_{60}, C_{60}-700, and C_{60}-750 (Fig. S1a) are well-matched to the standard XRD pattern of C_{60} crystal (JCPDS NO. 81-2220), indicitating the well maintaintion of structrue of C_{60} at temperatures of ≤ 750 °C. Similarly, as shown in Fig. S1b, it could be seen that Raman spectra of C_{60} and C_{60}-Ts samples at 700 and 750 °C presents the characteristic peaks of C_{60} such as Hg (eight fivefold-degenerated modes of symmetry) and Ag (two nondegenerate modes of symmetry). [1. *Adv. Mater*. **2017**, 29, 1603414.; 2. *Phil. Trans. R. Soc. Lond. A* **2004**, 362, 2375–2406] But the characteristic peaks of C_{60} were disappeared in C_{60}-780 sample. Above all, the C_{60}-T samples remain the crystal structure of C_{60} at the carbonization temperatures of ≤ 750 °C. However, when the temperature was increased to 780 °C, all the peaks belong to C_{60} in both the XRD pattern and Raman spectra disappear, indicating the break of the C_{60} cages and the formation of HCs. So we chose 780 °C as the lowest carbonization temperature for our investigation.

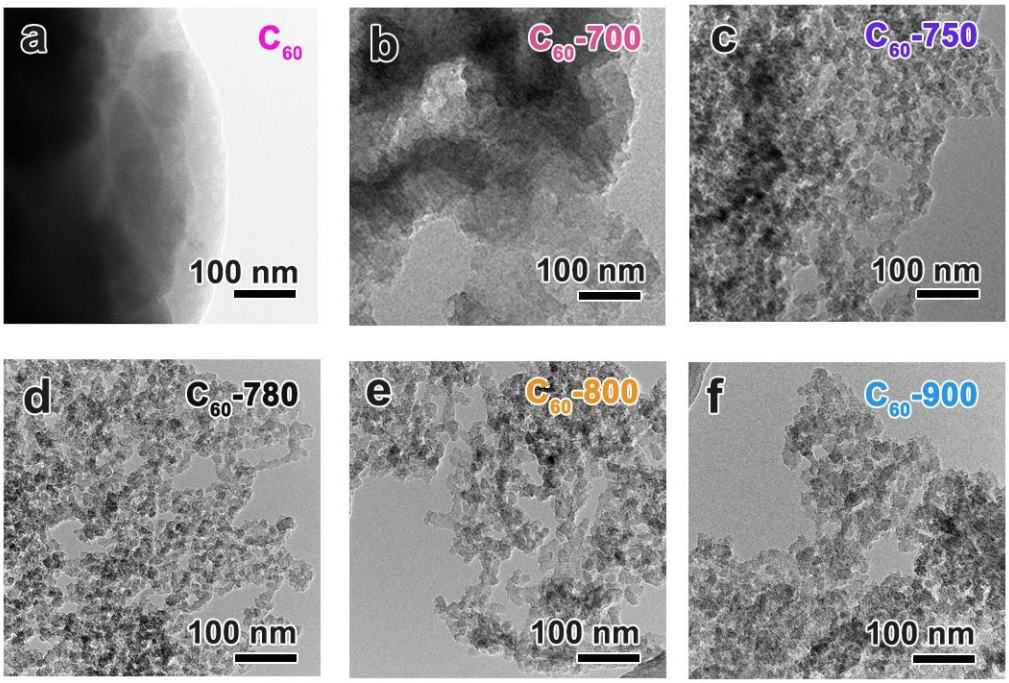

Fig. S2 The microstructure evolution of C_{60}-T samples. The low-magnification TEM images of **a** C_{60}; **b** C_{60}-700; **c** C_{60}-750; **d** C_{60}-780; **e** C_{60}-800; and **f** C_{60}-900.

To vividly investigate the microstructure evolution of C_{60} and C_{60}-Ts, the low-magnification TEM images of from C_{60} to C_{60}-900 were shown in Fig. S2. It could be seen that, as shown in Fig. S2a ~ c, there are few pores in C_{60} indicating the bulk structure, while the C_{60}-700 and C_{60}-750 samples gradually exhibit more and more pores due to the slight broken and decomposition of C_{60}, which is correspond to macro-porous structure appearance of C_{60}-750 sample. Besides, the cross-linked nanoparticles of 20 to 30 nm seem to become a bit thin from C_{60}-750 to C_{60}-780 (Fig. S2c and S2d), which may be attribute to the structure transformation from C_{60} to hard carbon. However, with the further increase the temperature to 800, the C_{60}-800 exhibits the particle aggregation, which may be attributed to the reconstruction of carbon structure.

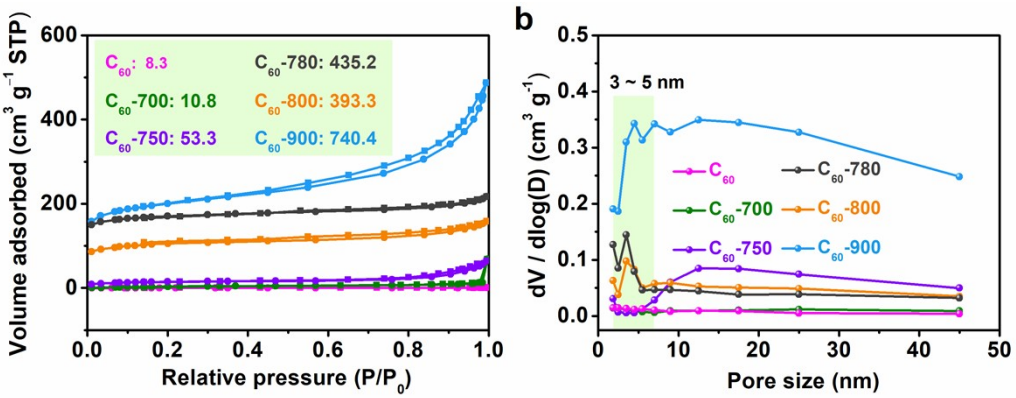

Fig. S3 The evolution of the specific surface area and pore structure C_{60}-T samples. a Nitrogen adsorption/desorption isotherms and **b** BJH pore size distributions of C_{60} and C_{60}-Ts.

Nitrogen adsorption-desorption isotherms were used to examine the evolution of specific surface area (SSA) and pore structure of C_{60}-Ts with the increase of the pyrolyzed temperature. As shown in Fig. S3a, the SSA of C_{60}, C_{60}-700, and C_{60}-750 samples gradually increase from 8.3 to 53.3 m^2 g^{-1} (Fig. S3a), and the macro-porous structure gradually appears from C_{60} to C_{60}-750 (Fig. S3b). However, when the annealing temperature reached to 780 °C, the SSA of C_{60}-780 drastically increases to 435.2 m^2 g^{-1} and the macro-porous structure is fully transfer to the mesoporous structure from C_{60}-750 to C_{60}-780, which may be attributed to the transformation of the structure from C_{60} to hard carbon. With the further increase of the carbonization temperature to 800 °C, the SSA of C_{60}-800 decreases slightly to 393.3 m^2 g^{-1}, which may be attributed to the particle aggregation, which is corresponded to the results of the low-magnification TEM images as shown in Fig. S2.

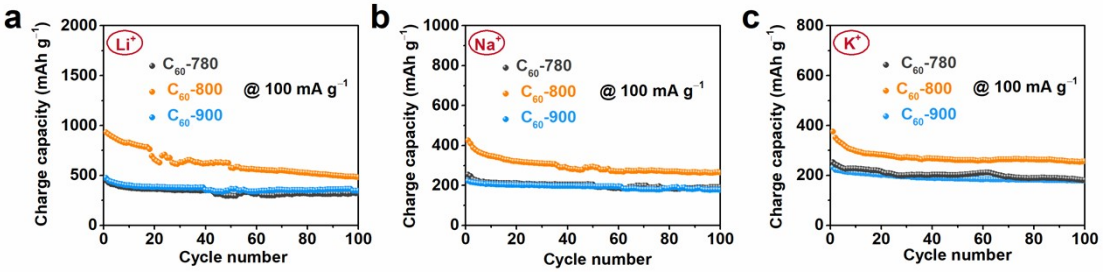

Fig. S4 The cycling performance of C_{60}-Ts (T = 780, 800 and 900 °C) at a current density of 100 mA g^{-1} for **a** Li^+, **b** Na^+, and **c** K^+ storage.

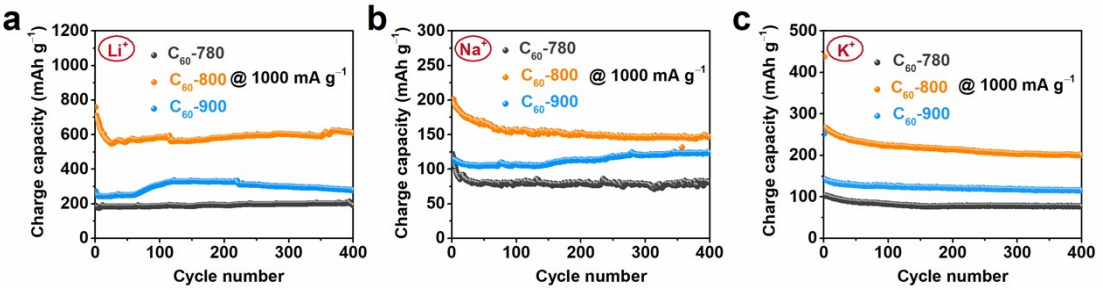

Fig. S5 The cycle performance of C_{60}-T (T = 780, 800 and 900 °C) at a current density of 1000 mA g^{-1} for **a** Li^+, **b** Na^+, and **c** K^+ storage.

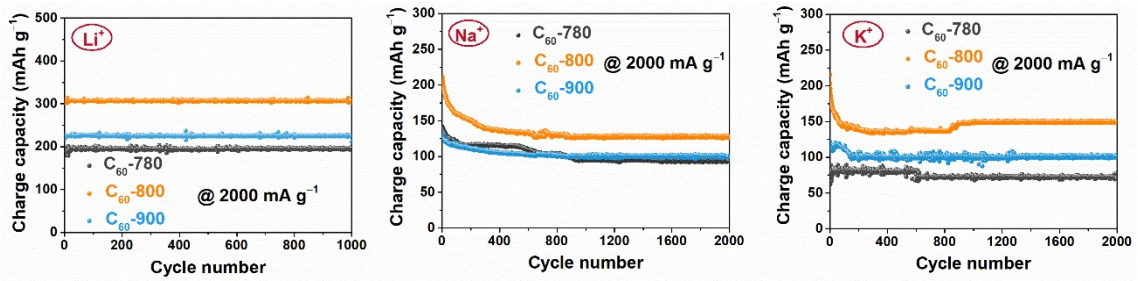

Fig. S6 The cycle performance of C_{60}-T (T = 780, 800 and 900 °C) at a current density of 2000 mA g^{-1} for **a** Li^+, **b** Na^+, and **c** K^+ storage.

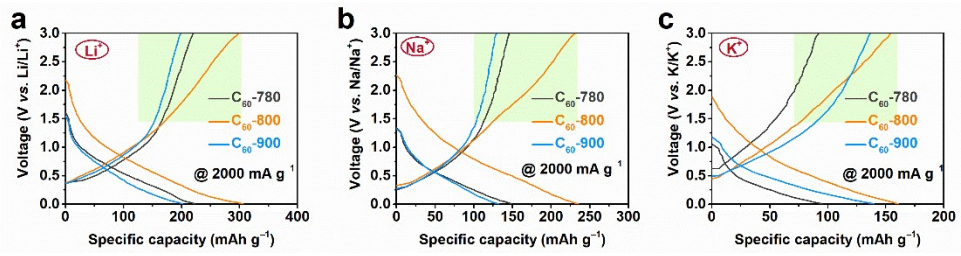

Fig. S7 The comparison of galvanostatic discharge/charge curves of C_{60}-Ts at a current rate of 2000 mA g^{-1} for **a** Li^+, **b** Na^+, and **c** K^+ storage.

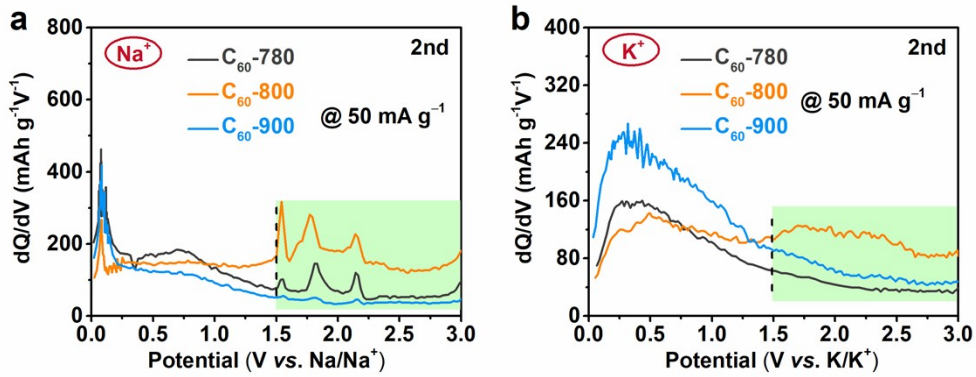

Fig. S8. The dQ/dV curves of C_{60}-Ts (T = 780, 800, and 900 °C) at the second cycle at 50 mA g^{-1} for **a** Na^+ and **b** K^+ storage.

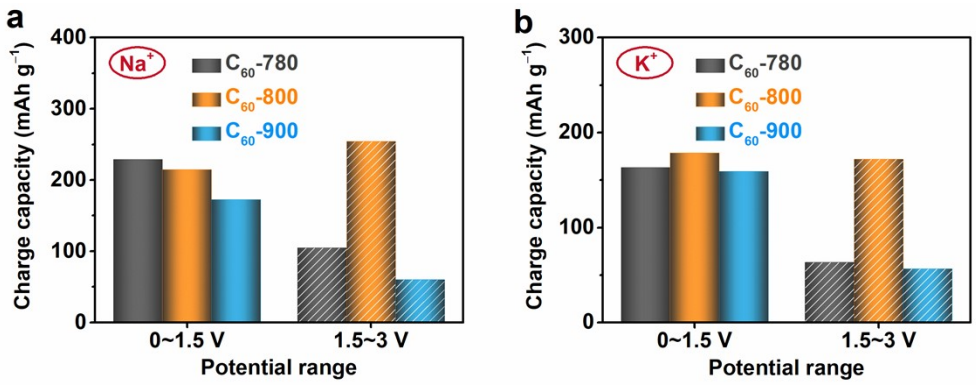

Fig S9. The charge capacities of C_{60}-Ts (T = 780, 800, and 900) in 0.01 ~ 1.5 V and 1.5 ~ 3.0 V for **a** Na^+ and **b** K^+ storage.

Table S1. The typical characteristics of C_{60}-Ts samples including interlayer distance (d_{002}), SSA, and defect degree. d_{002} represents the interlayer distance of 002 plane based on XRD results; S_{BET} is the specific surface area calculated by the Brunauer–Emmett–Teller (BET) method; the defect degree is estimated by the intensity ratio of D band and G band in Raman spectra.

Sample	d_{002}	S_{BET} (m^2 g^{-1})	Defect degree
C_{60}-780	0.48	435.2	0.96
C_{60}-800	0.44	393.3	1.03
C_{60}-900	0.40	740.4	1.06
C_{60}-1000	0.38	647.3	1.10

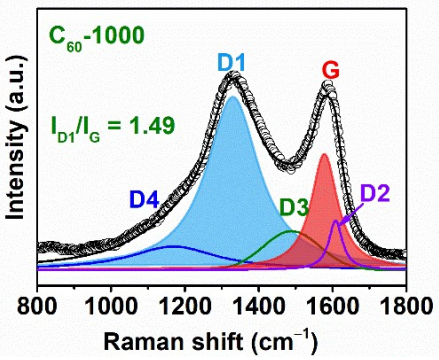

Fig. S10. Raman spectra and corresponding fitted curves of the C_{60}-1000.

Raman spectra of C_{60}-1000 (Fig. S10) show broad D- and G-band peaks, which could be deconvoluted into five peaks with Gaussian-Lorentzian numerical simulation. Similarly, The D1 band (1330 cm^{-1}), D2 band (1608 cm^{-1}), and D3 band (1489 cm^{-1}) could be assigned, respectively, to the A_{1g} symmetry vibration of the graphene layer edges, E_{2g} symmetry vibration of the surface graphene layers, and the short-range sp^3-C vibration of the amorphous carbon. The D4 band at 1169 cm^{-1} arises from the sp^2-sp^3 bonds or C–C and C=C stretching vibrations polyene-like structures. The intensity ratio of D1 to G band (I_{D1}/I_G) is always used to measure the fraction of the sp^2-C at the exposed graphene layer edges. The calculated I_{D1}/I_G of C_{60}-1000 is 1.49, demonstrating the percentage of the sp^2-C in C_{60}-800 is the lowest. Besides, the ratio of sp^3 and sp^2-hybridized carbon of C_{60}-1000, estimated by the integral area ratio of fitting Raman spectra, is 0.271, also indicating the highest sp^3-C fraction of C_{60}-800, which agrees with the XPS results as summarized in Fig. 3g.

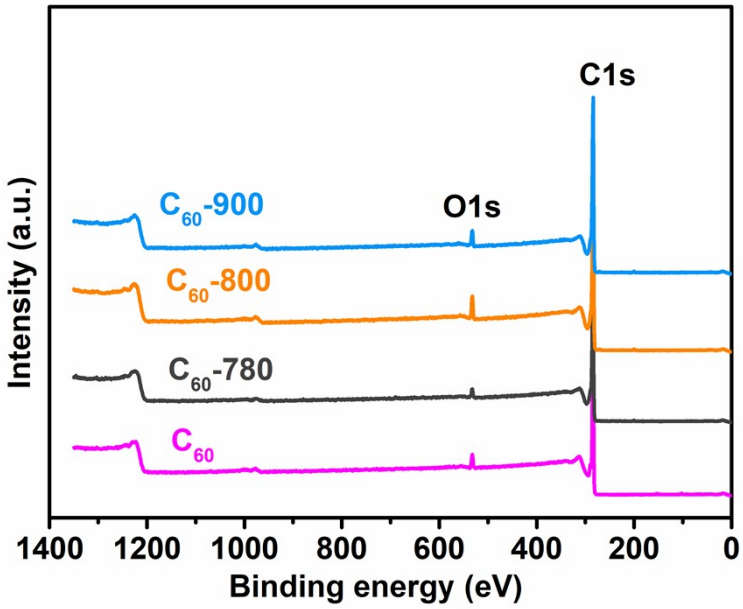

Fig. S11. The XPS survey spectra of C_{60} and C_{60}-Ts.

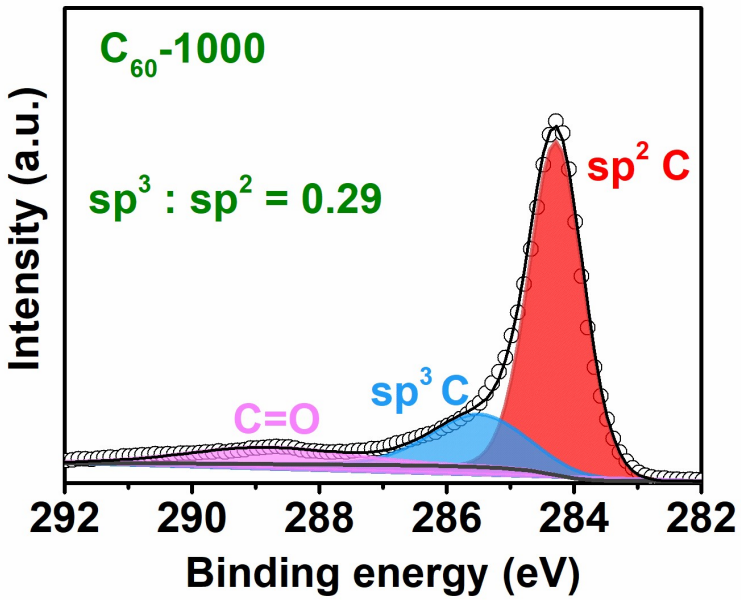

Fig. S12. the high-resolution C1s XPS spectra and corresponding fitted curves of C_{60}-1000.

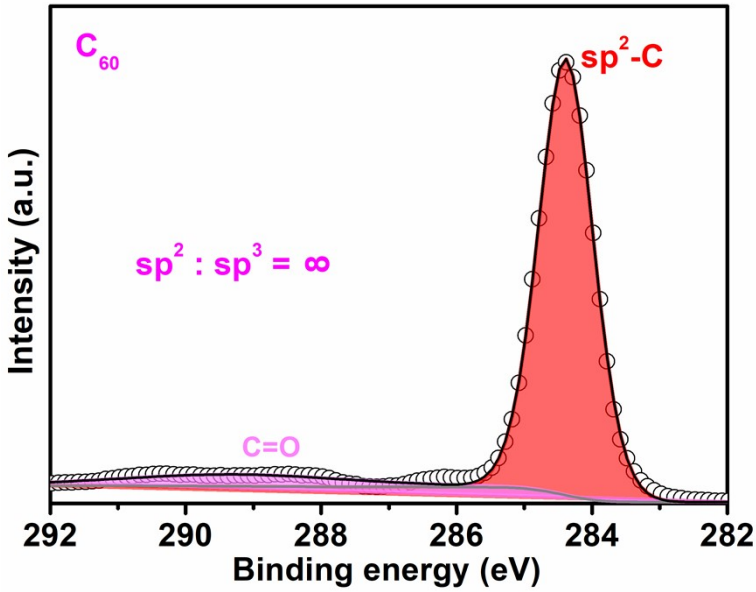

Fig. S13. The high-resolution C1s XPS spectra and corresponding fitted curves of C_{60}.

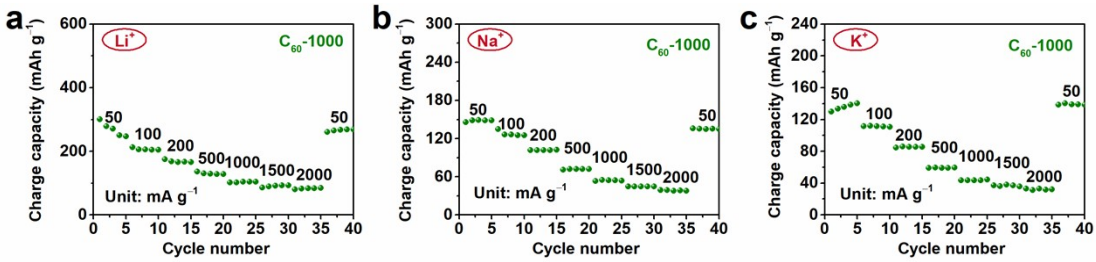

Fig. S14. The rate capability of C_{60}-1000 at current densities of 50, 100, 200, 500, 1000, 1500, and 2000 mA g^{-1} for **a** Li^+, **b** Na^+, and **c** K^+ storage.

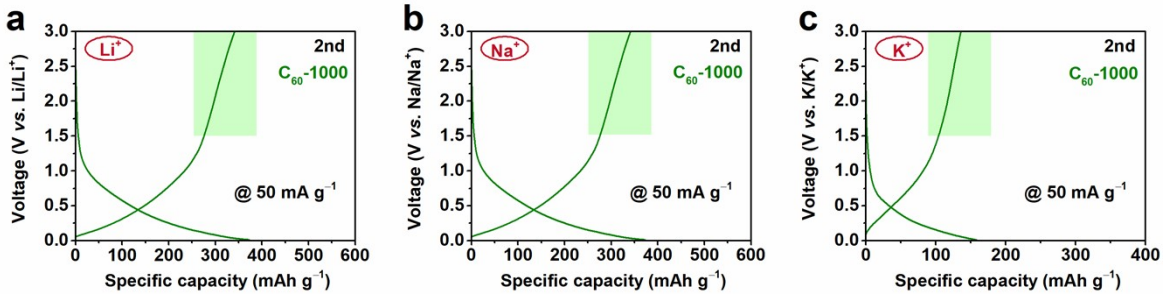

Fig. S15. The second charge-discharge curves of C_{60}-1000 at current densities of 50 mA g^{-1} for **a** Li^+, **b** Na^+, and **c** K^+ storage.

Quantitative analysis of Na^+-ions storage behaviors in C_{60}-Ts (T = 780, 800, and 900).

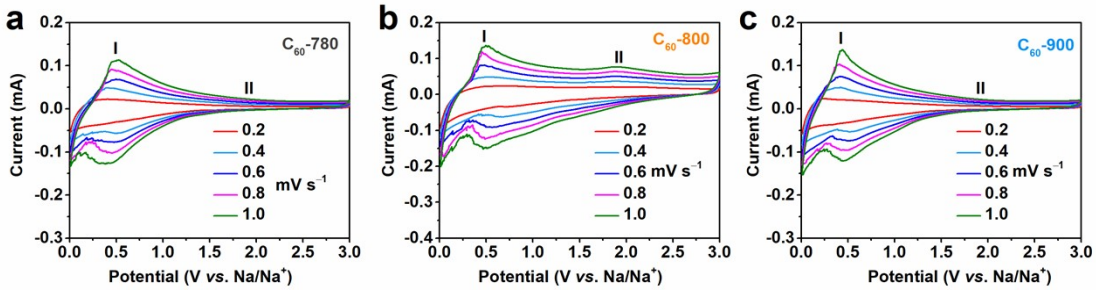

Fig. S16 The CV curves of **a** C_{60}-780, **b** C_{60}-800, and **c** C_{60}-900 at scan rates of 0.1 to 1.0 mV s^{-1}.

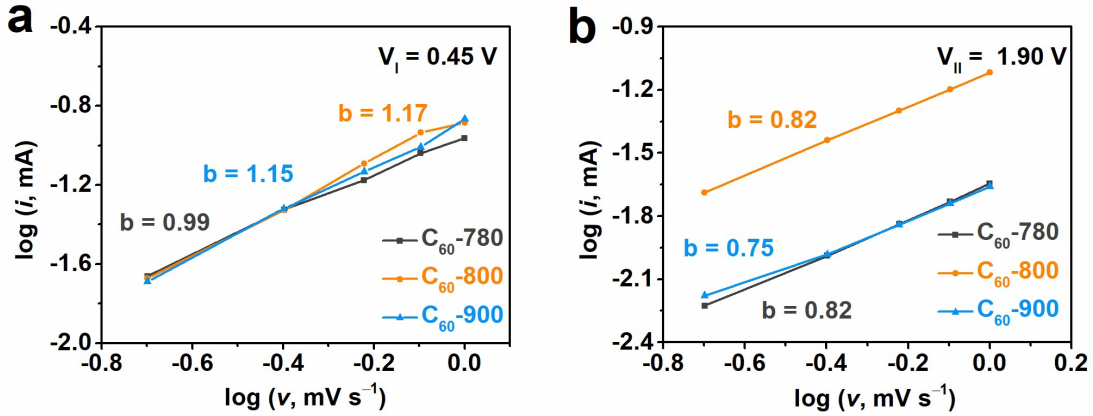

Fig. S17 The Log(*i*)–log(*v*) curves (b-value determination) of C_{60}-Ts at **a** 0.45 V and **b** 1.90 V.

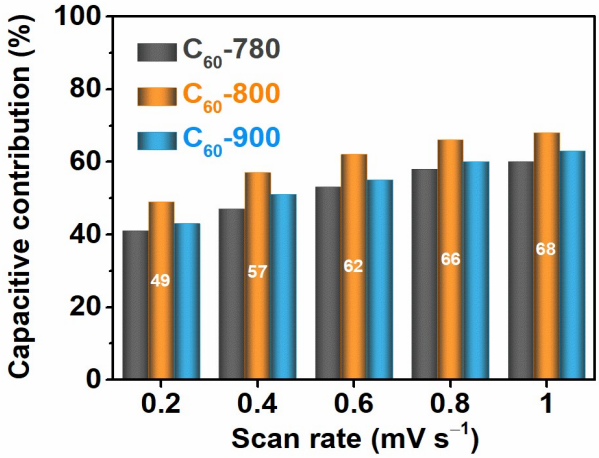

Fig. S18 The capacitive contributions of C_{60}-Ts at different scan rates.

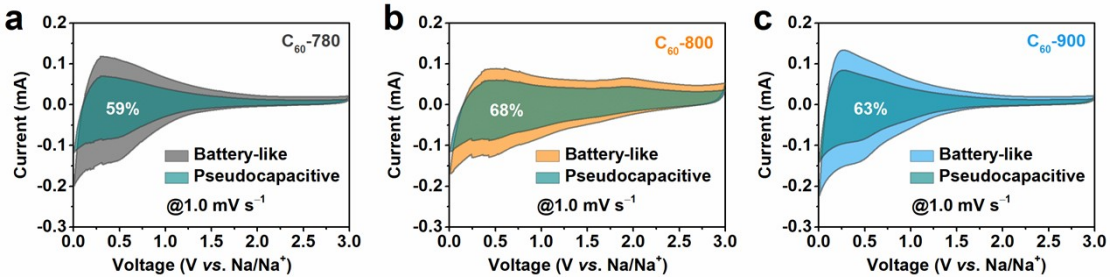

Fig. S19 The capacitive contribution of **a** C_{60}-780, **b** C_{60}-800, and **c** C_{60}-900 at a scan rate of 1.0 mV s^{-1}.

Quantitative analysis of K^+-ions storage behaviors in C_{60}-Ts (T = 780, 800, and 900).

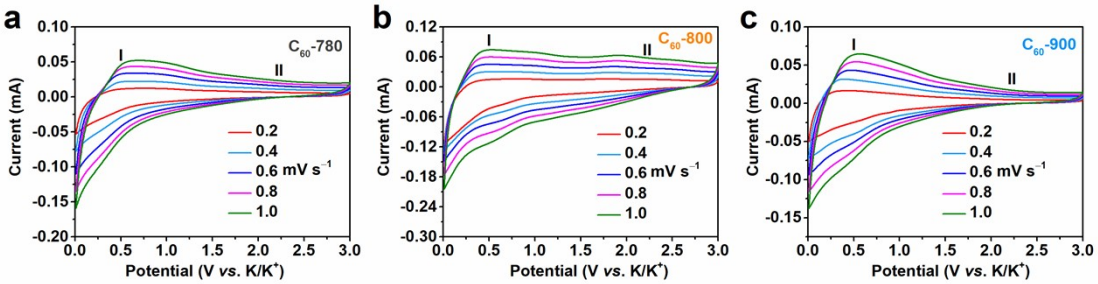

Fig. S20 The CV curves of **a** C_{60}-780, **b** C_{60}-800, and **c** C_{60}-900 at scan rates of 0.1 to 1.0 mV s^{-1}.

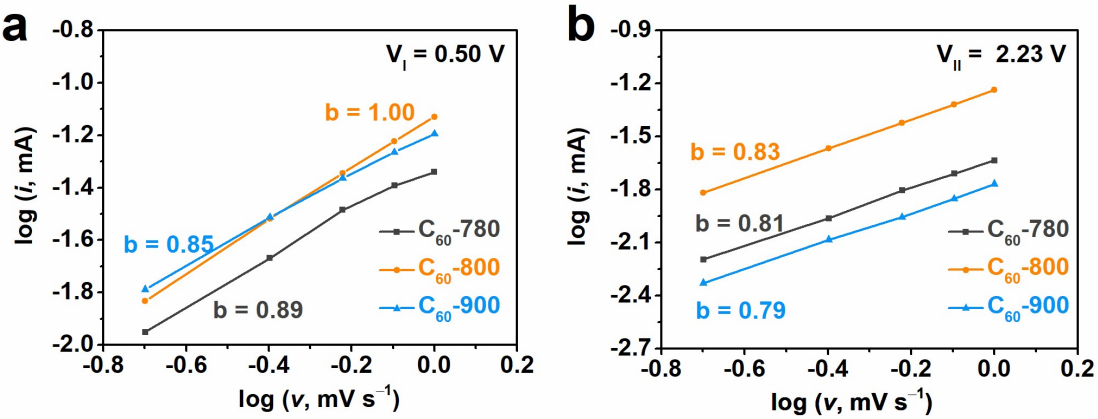

Fig. S21 The Log(*i*)–log(*v*) curves of C_{60}-Ts at **a** 0.50 V and **b** 2.23 V.

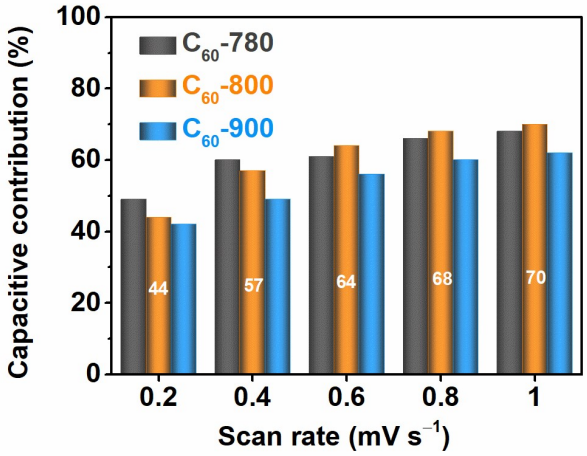

Fig. S22 The capacitive contributions of the C_{60}-Ts at different scan rates.

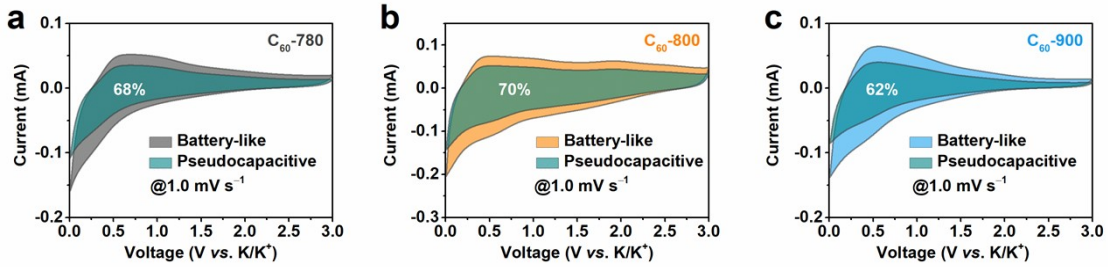

Fig. S23 The capacitive contribution of **a** C_{60}-780, **b** C_{60}-800, and **c** C_{60}-900 at a scan rate of 1.0 mV s^{-1}.

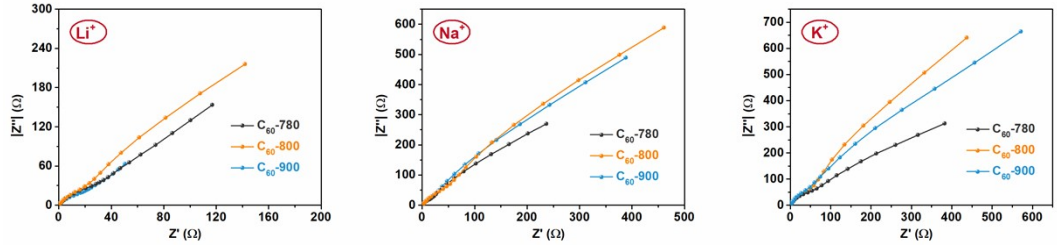

Fig. S24 The EIS spectra of the C_{60}-780, C_{60}-800, and C_{60}-900 electrodes for (a) Li^+, (b) Na^+, (c) K^+ after cycling at a high current density of 2000 mA g^{-1}.

Electrochemical impedance spectroscopy (EIS) is a powerful technique for investigating processes occurring in electrochemical systems. Generally, such processes involve the dynamics of bound or mobile charges in the bulk or interfacial regions of solid material. We measured the EIS spectra after cycling at a high current density of 2000 mA g^{-1} and added them as shown in Fig. S24. The impedance plots shown in Fig. S24 can be divided into a high-frequency component (partial semicircle) and a low-frequency component (straight slopping line along the imaginary axis). The semicircle in the high-frequency range is associated with the surface properties of the electrode and corresponds to the Faradic charge-

transfer resistance. The charge transfer resistance is directly related to the electroactive surface area (the combination of electrolyte accessible area and electrical conductivity of the electrode materials. It could be seen that the c_{60}-800 shows the smallest radius among the three samples. In addition, the low-frequency part is related to the ions diffusion. Thus, the alkali ion diffusion (Li^+, Na^+, and K^+) coefficient, D_{ions}, can be calculated from the Warburg region using equation (1): [1. *Energy Environ. Sci.*, **2012**, 5, 9595.; 2. *ACS Appl. Mater. Interfaces*, **2016**, 8, 18788.]

$$D = \frac{R^2T^2}{2A^2n^4F^4C^2\sigma_w^2} \#(1)$$

where R is the universal gas constant, T is the absolute temperature, F is the Faraday constant, n is the number of electrons, A is the electrode area of the electrode and C is the concentration of lithium ions in the electrolyte (10^{-3} mol cm^{-3}). According to equation (2), σ_w is the Warburg factor, and ω is the angular frequency, which is related to Z′ and can be attained from the slope of the fitting line of the EIS data (Fig. 25) at low frequencies: [3. *Energy Storage Materials*, **2018**, 11, 161.]

$$Z' = R_e + R_{ct} + \sigma_\omega \frac{1}{\sqrt{\omega}} \#(2)$$

The ions diffusion coefficients (D_{ions}, cm^2 s^{-1}) of all the cells are calculated using equation (1) and (2), which are shown in Table S2. The D_{ions} of the C_{60}-800 with higher sp^3-hybridized carbon atoms are higher than that of C_{60}-780 and C_{60}-900, indicating the existence of sp^3-hybridized carbon atoms could accelerate the alkali ions diffusions and storage. These results are in accordance with the simulation results.

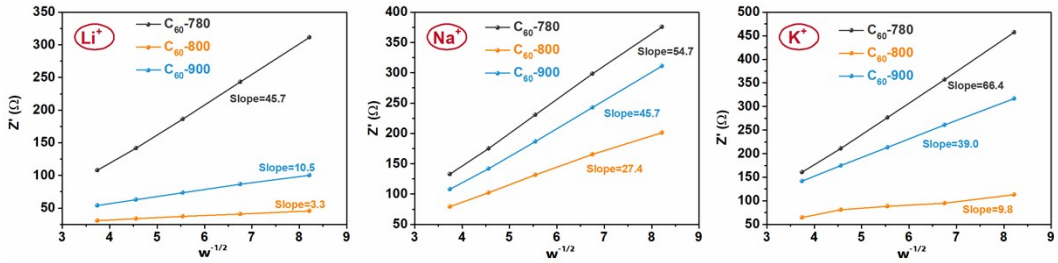

Fig. S25 Z′ as a function of the $\omega^{-1/2}$ plot in the low frequency range (the slope of fitting curves is the Warburg factor, σ_ω)

Table S2 The alkion ions (Li^+, Na^+, and K^+) diffusion coefficients of C_{60}-780, C_{60}-800, and C_{60}-900 electrodes.

Sample	C_{60}-780	C_{60}-800	C_{60}-900
$D_{Li+}/cm^2\ s^{-1}$	2.75×10^{-14}	5.41×10^{-12}	5.20×10^{-13}
$D_{Na+}/cm^2\ s^{-1}$	1.93×10^{-14}	7.65×10^{-14}	2.75×10^{-14}
$D_{K+}/cm^2\ s^{-1}$	3.78×10^{-14}	5.96×10^{-13}	1.30×10^{-14}

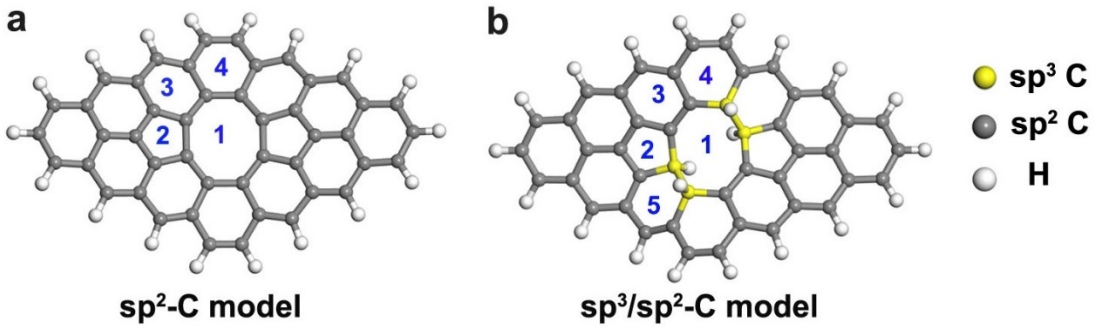

Fig. S26 The theoretical carbon models and adsorption sites of **a** sp^2-C and **b** sp^3/sp^2-C model.

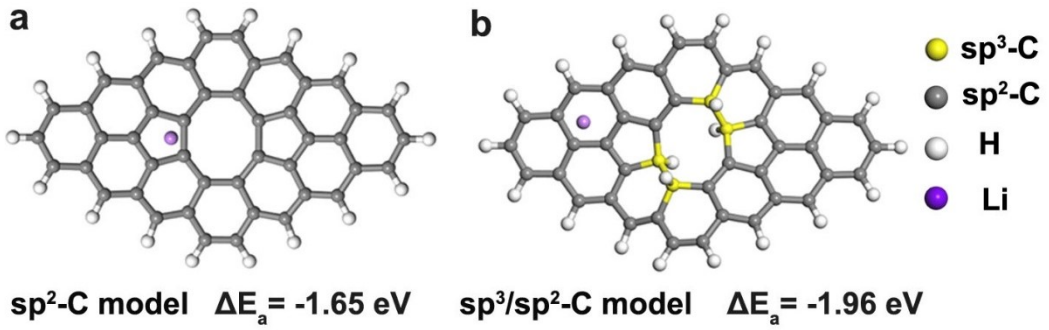

Fig. S27 The optimized geometry of the **a** sp^2-C and **b** sp^3/sp^2-C model with an adsorbed lithium atom and corresponding adsorption energy.

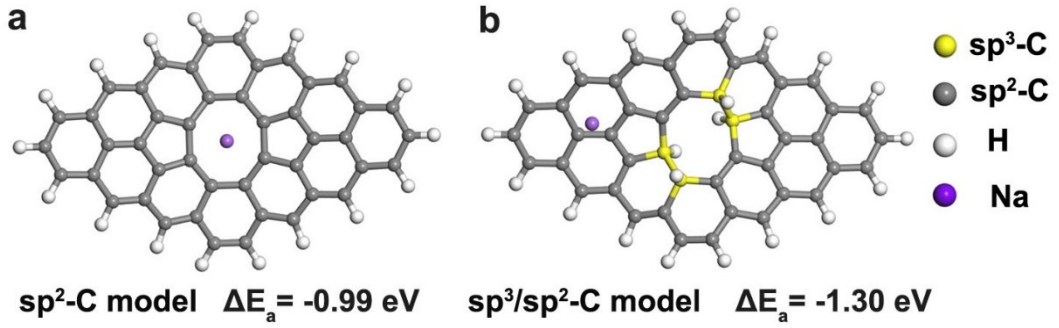

Fig. S28 The optimized geometry of the **a** sp^2-C and **b** sp^3/sp^2-C model with an adsorbed sodium atom and corresponding adsorption energy.

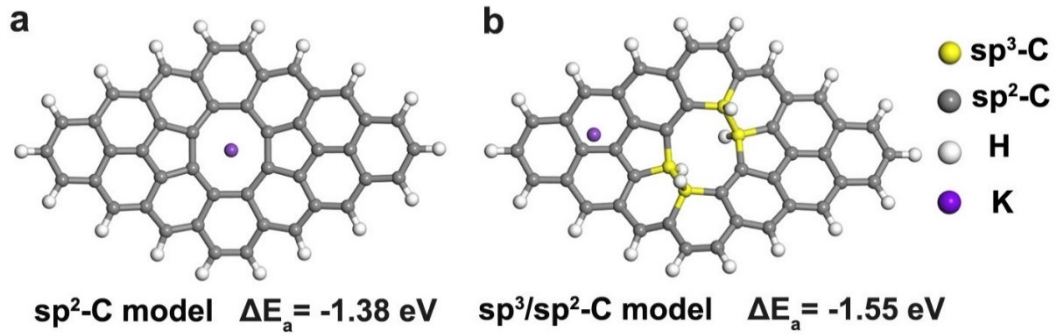

Fig. S29 The optimized geometry of the **a** sp^2-C and **b** sp^3/sp^2-C model with an adsorbed potassium atom and corresponding adsorption energy.